

# Short-Range Order Based Ultra Fast Large-Scale Modeling of High-Entropy Alloys

Caimei Niu<sup>a</sup>, Lifeng Liu<sup>b,\*</sup>

<sup>a</sup>*School of Software and Microelectronics, Peking University, Beijing, China*

<sup>b</sup>*School of Integrated Circuits, Peking University, Beijing, China*

---

## Abstract

High-Entropy Alloys (HEAs) exhibit complex atomic interactions, with short-range order (SRO) playing a critical role in determining their properties. Traditional methods, such as Monte Carlo (MC) based ATAT and SCRAPs, and hybrid Monte Carlo-Molecular Dynamics (MC-MD), are often constrained by system size and computational inefficiency, limiting their applicability for large-scale modeling. We introduce PyHEA, a Python based toolkit with a high-performance C++ core, designed to efficiently model HEAs through a combination of global and local search algorithms, incremental SRO calculations, and GPU acceleration. PyHEA delivers an impressive speedup of more than 333,000× and 10,000× over state-of-the-art tools ATAT and SCRAPs respectively, ensuring accurate SRO calculations with unprecedented efficiency. In practical applications, PyHEA successfully modeled a 256,000-atom Fe-Mn-Cr-Co alloy, replicating literature results and reducing computational time from days to seconds with GPU acceleration, achieving over 1,000× speedup compared to hybrid MC-MD approaches. This huge breakthrough in computational efficiency revolutionizes HEA modeling by bridging theoretical predictions and practical applications, opening new horizons for the design of next-generation HEAs.

*Keywords:* High-Entropy Alloys, Short-Range Order, High Performance Computing, Monte Carlo Search, Molecular Dynamics, GPU acceleration

---

## 1. Introduction

High-Entropy Alloys (HEAs), introduced by Jien-Wei Yeh et al. in 2004 [1], have emerged as a transformative class in materials science. Characterized by the

---

\*Corresponding author

*Email addresses:* caimeiniu@stu.pku.edu.cn (Caimei Niu), lfliu@pku.edu.cn (Lifeng Liu)

presence of five or more principal elements in quasi-equimolar ratios (typically 3 to 55% atomic percent each), HEAs exhibit a unique combination of remarkable properties, including high strength, hardness and exceptional resistance to oxidation and corrosion [2, 3, 4, 5]. These attributes position HEAs as promising materials for applications in extreme environments, such as aerospace, nuclear, and energy sectors. Furthermore, the unconventional nature of HEAs challenges traditional alloy design theories, which spurred significant research interest in their underlying principles [6, 7].

Recent advancements have highlighted the critical role of microstructure in determining HEAs’ extraordinary properties, particularly the influence of short-range order (SRO) [8, 9]. SRO refers to the local atomic arrangement within an alloy, a phenomenon that becomes increasingly prominent in complex concentrated alloys, even under rapid solidification conditions [11, 13]. The impact of SRO on mechanical performance and thermal stability is profound, influencing elastic modulus, stiffness, and ductility by optimizing the balance between strength and toughness [14, 15, 16]. These findings underscore the potential for leveraging SRO control to tailor HEA properties, providing a theoretical framework for the development of new high-performance materials.

The primary challenge in designing HEAs with precise SRO control lies in the vast configurational space. For an equiatomic HEA with  $N$  total atoms and  $M$  different principal elements, the configurational space size  $\Omega$  is given by:

$$\Omega = \frac{N!}{\left(\frac{N!}{M!}\right)^M}. \quad (1)$$

This expression reveals the astronomical complexity of the problem—even a modest Cantor alloy (CrMnFeCoNi) with just 250 atoms yields approximately  $10^{170}$  possible configurations [17, 18]. Moreover, realistic applications demand simulations of tens or even hundreds of thousands of atoms to fully capture mechanical and structural properties [33], further amplifying this complexity.

Current approaches to HEA modeling face significant limitations in addressing this challenge. Static structure construction methods, such as ATAT [21, 42, 22] and SCRAPS [23], rely on Special Quasirandom Structures (SQS) and hybrid Monte Carlo approaches, respectively, to generate random alloy configurations. While effective for handling relatively small supercells (tens to hundreds of atoms), these methods become computationally prohibitive for larger systems [20] and fail to capture critical SRO effects, particularly at lower temperatures where atomic ordering significantly influences material properties [24, 25, 26].

Hybrid Monte Carlo-Molecular Dynamics (MC-MD) methods offer an alternative

approach by incorporating MC steps into extended MD simulations. Although hybrid MC-MD can theoretically handle systems with hundreds of thousands of atoms [27, 17, 28], its practical effectiveness depends heavily on the availability of highly accurate interatomic potentials. Even when such potentials exist, generating configurations that reliably reflect SRO demands substantial computational resources, often requiring hours or days of calculation time.

To address these challenges, we introduce PyHEA, a high-performance computational framework that revolutionizes large-scale HEA modeling through three key innovations:

- **Enhanced accuracy and versatility:** PyHEA significantly outperforms existing methods like ATAT and SCRAPs in both modeling efficiency and stability. Our benchmarks in [Table 1](#) demonstrate up to 333,000 and 13,900 times speedup compared with ATAT and SCRAPs respectively while maintaining or improving accuracy. Unlike current tools that primarily generate random configurations, PyHEA supports user-defined target SRO values, making it uniquely suitable for modeling temperature-dependent ordering effects and other practical scenarios where specific atomic arrangements are desired.
- **Unprecedented scalability and speed:** Through advanced GPU acceleration (CUDA) and optimized search algorithms, PyHEA efficiently handles systems with hundreds of thousands of atoms. For example, it successfully modeled a 256,000-atom Fe-Mn-Cr-Co system in under 40 seconds—a task that typically requires hours or days using traditional hybrid MC-MD method. The details of the hybrid MC-MD simulations are elaborated in [section 4](#). This breakthrough in computational efficiency enables the exploration of mechanical properties and structural characteristics at previously inaccessible scales.
- **Comprehensive software ecosystem:** Built on Python with a high-performance C++ core, PyHEA combines accessibility with computational efficiency. Released under the LGPL-3.0 license, it provides an end-to-end solution including structure generation, SRO optimization, and analysis tools. The modular design facilitates easy integration with existing workflows and enables rapid customization for specific research needs.

In the following sections, we detail PyHEA’s methodology, demonstrate its performance advantages through comprehensive benchmarks, and showcase its practical applications in a large scale HEA system. Our results establish PyHEA as a transformative tool that bridges the gap between theoretical understanding and practical

simulation of large-scale HEA systems, opening new possibilities for materials design and optimization.

## 2. Results

### 2.1. Parameter Optimization Analysis

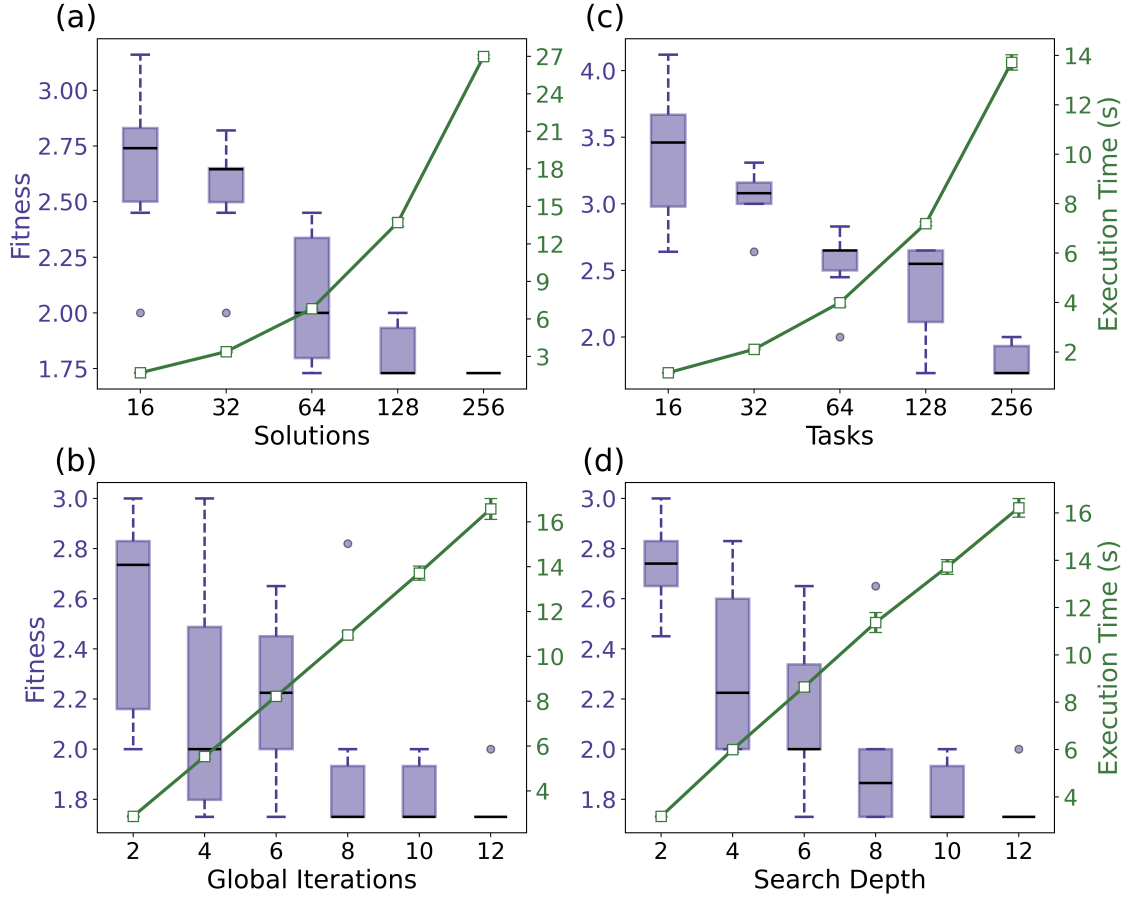


Figure 1: Influence of input parameters on fitness and execution time. (a) Number of solutions, (b) global iterations, (c) number of tasks, and (d) search depth. The plots illustrate the impact of varying each parameter on the fitness (left axis) and execution time (right axis).

In optimizing atomic configurations for HEAs, several key parameters significantly influence both the quality of results and computational efficiency. These parameters include: the number of solutions (which determines the population size for exploring different atomic arrangements), global iterations (controlling how many

times the entire optimization process is repeated), number of tasks (affecting the degree of parallelization in the search process), and search depth (determining how thoroughly each local configuration is explored). Each parameter plays a distinct role in the search algorithm detailed in [subsection 4.1](#) and [subsection 4.2](#). Understanding their optimal values is crucial for achieving the best balance between computational efficiency and solution quality.

To evaluate optimization quality, we employ a fitness function that quantifies how well atomic configurations align with the target Short-Range Order (SRO) characteristics. Lower fitness values indicate better alignment with desired SRO properties. Our analysis reveals distinct patterns in how each parameter affects both fitness and computational efficiency.

As depicted in [Fig. 1\(a-b\)](#), an increase in the number of solutions improves fitness; however, beyond 64 solutions, this enhancement yields diminishing returns while causing a marked rise in execution time. A similar pattern emerges for global iterations, where substantial fitness improvements are observed up to 6 iterations. Beyond this threshold, further gains are minimal, whereas execution time continues to escalate. These results indicate that using 64 to 128 solutions and 6 global iterations achieves an effective balance between precision and computational cost.

Parallelism also plays a critical role in the optimization process. As demonstrated in [Fig. 1\(c\)](#), increasing the number of tasks enhances the consistency of fitness outcomes. Nevertheless, execution time grows significantly after 128 tasks, with only marginal improvements in fitness. Therefore, a task count between 64 and 128 represents an optimal range. Similarly, [Fig. 1\(d\)](#) shows search depth affects the thoroughness of exploration within each iteration. Deeper searches (greater than 8) yield better fitness values, they also come at the expense of increased computational demands. Based on these findings, a search depth of 8-10 strikes an optimal balance between precision and computational efficiency.

Consequently, we recommend two parameter configurations optimized for different priorities. The precision-optimized configuration (128 solutions, 10 global iterations, 256 tasks, search depth 10) achieves maximum accuracy in SRO calculations. The performance-optimized configuration (64 solutions, 6 global iterations, 64 tasks, search depth 8) maintains good optimization quality while reducing computation time as much as possible. Users can select either configuration based on their specific requirements for precision versus computational efficiency.

## *2.2. Comparison with State-of-the-Art Methods*

To evaluate the performance of PyHEA, we conducted a comparative analysis against SCRAPS [23], a state-of-the-art method commonly utilized in HEA model-

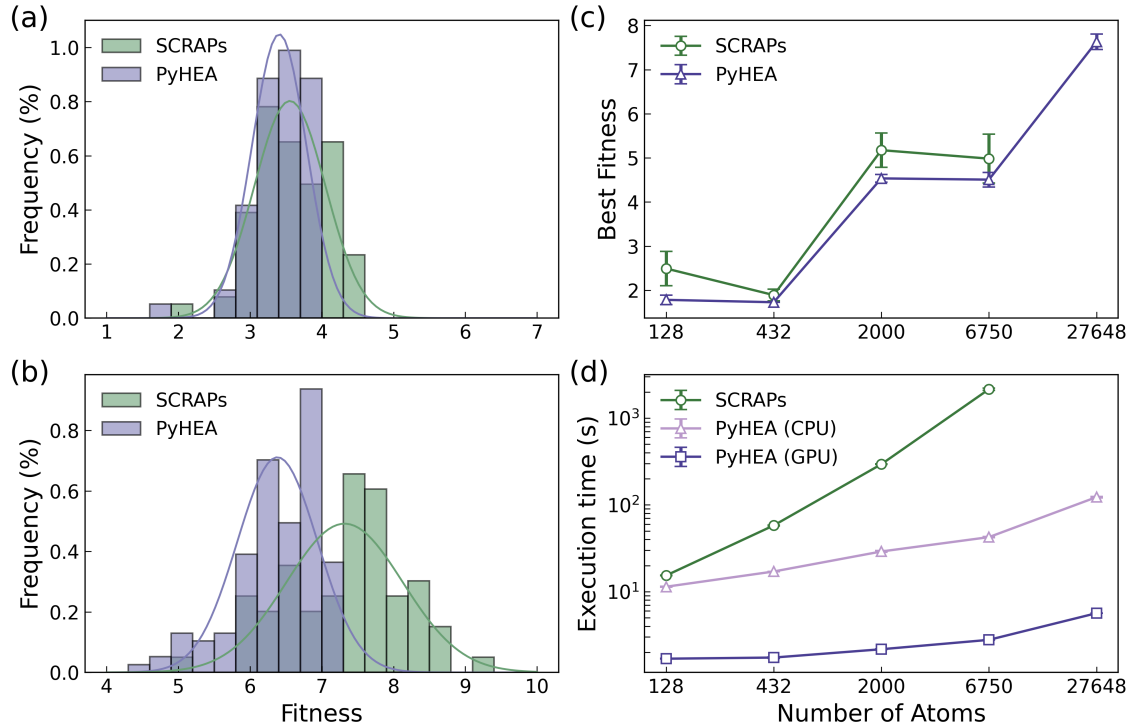


Figure 2: Comparison of PyHEA and SCRAPs in terms of fitness accuracy and execution time. (a) and (b) show the distribution of fitness values (lower values indicate higher accuracy) for systems containing 128 atoms and 2000 atoms, respectively. (c) illustrates the best fitness values as a function of system size. (d) presents the execution times for SCRAPs, PyHEA (CPU), and PyHEA (GPU) across various system sizes. Both SCRAPs and PyHEA (CPU) were tested on the same CPU cluster equipped with an Intel Xeon Gold 6132 CPU @ 2.60 GHz using 24 processors, while PyHEA (GPU) utilized an NVIDIA 4090 GPU.

ing. This comparison focused on evaluating both fitness quality and computational efficiency across varying system sizes.

Fig. 2(a-b) present the fitness distributions for typical bcc configurations with 128 atoms and 2000 atoms, respectively. PyHEA consistently exhibits a more concentrated fitness distribution compared to SCRAPs, particularly as the system size increases. In the case of the 2000-atom system, PyHEA demonstrates a narrower spread with a higher peak frequency around the optimal fitness value, signifying more stable and reliable outcomes. Conversely, SCRAPs shows a broader distribution of fitness values, indicating that PyHEA’s optimization strategy is more robust, especially in larger systems.

The enhanced fitness quality of PyHEA is further corroborated by Fig. 2(c),

which tracks the optimal fitness values as system size increases. While PyHEA and SCRAPs achieve comparable fitness levels for smaller systems (e.g., 128 and 432 atoms), PyHEA surpasses SCRAPs as the system size exceeds 2000 atoms, highlighting its scalability and the effectiveness of its optimization approach. This is particularly crucial for large-scale HEA simulations where fitness convergence is increasingly challenging.

A key advantage of PyHEA is its computational efficiency, particularly with GPU acceleration. [Fig. 2\(d\)](#) compares the execution times of PyHEA (in both CPU and GPU implementations) and SCRAPs as a function of system size. SCRAPs faces significant scalability challenges, with execution times increasing rapidly as the system size grows. Notably, SCRAPs becomes computationally prohibitive at approximately 6750 atoms, beyond which further calculations are unfeasible.

In contrast, PyHEA’s GPU implementation seamlessly handles larger system sizes. At the largest system size of 27,648 atoms, PyHEA’s GPU-accelerated version achieves a performance improvement of four orders of magnitude compared to SCRAPs. This significant boost in computational efficiency allows PyHEA to handle system sizes that are beyond the practical capacity of SCRAPs.

To further validate PyHEA’s acceleration benefits, we also conducted a comparison with another widely used MC-based tool, ATAT. [Table 1](#) summarizes the performance metrics based on serial execution across PyHEA (CPU and GPU), SCRAPs, and ATAT. While SCRAPs and ATAT perform comparably for smaller system sizes, they both struggle as the number of atoms increases. Like SCRAPs, ATAT becomes impractical beyond a few hundred atoms. Conversely, PyHEA’s GPU implementation maintains substantially lower execution times across all tested system sizes, underscoring its performance advantages and scalability. For a comprehensive comparison of parallel CPU performance between these tools, readers are referred to [Table A.2](#) in the Appendix.

### *2.3. Application*

To illustrate the practical potential of PyHEA, we conducted large-scale molecular dynamics (MD) simulations using LAMMPS, modeling a system containing 256,000 atoms of Fe-Mn-Cr-Co (composition: 40% Fe, 40% Mn, 10% Cr, and 10% Co) at various temperatures. The system was generated using PyHEA, enabling us to bypass the conventional Monte Carlo (MC) and MD hybrid process and achieve significant reductions in simulation time.

The system was simulated in an NPT ensemble for 10 ps, with the Radial Distribution Function (RDF) calculated to analyze the SRO behavior at different temperatures. As depicted in [Fig. 3](#), our results align closely with those from a reference study

Table 1: Performance comparison between PyHEA and existing methods (ATAT and SCRAPs) for optimizing atomic structures in high-entropy alloys, focusing on serial execution performance (parallel performance data available in Appendix). The table shows computation times (in minutes) and speedup ratios for both body-centered cubic (bcc) and face-centered cubic (fcc) structures across varying system sizes (#At) and numbers of species (#Sp). Both PyHEA and SCRAPs were executed in serial mode using a single CPU core (Intel Xeon Gold 6132 @ 2.60GHz), with additional GPU (NVIDIA 4090) results shown for PyHEA. The optimizations used 128 candidate solutions over 10 global iterations with 256 parallel MC tasks (search depth 10). Supercell sizes followed  $S = A \cdot L^3$ , where  $A = 2$  for bcc or  $A = 4$  for fcc structures. All calculations optimized short-range order (SRO) over 3 coordination shells. Dashes (–) indicate computationally infeasible cases, while speedup values are shown relative to SCRAPs[ATAT in brackets].

Type	#Sp	#At	ATAT	SCRAPs Serial	PyHEA Serial	PyHEA GPU	Speedup	
							CPU	GPU
bcc	3	54	>1.4k <sup>a</sup>	2.7	3.2	.03	.9[438]	98[47k]
bcc	4	128	>10k <sup>a</sup>	6.5	4.2	.03	1.6[2.4k]	233[333k]
bcc	4	432	–	24.2	5.6	.03	4.3	835
bcc	4	1024	–	103	6.2	.03	16.5	3.2k
bcc	4	2048	–	276	7.0	.04	39.4	7.9k
bcc	5	2048	–	286	9.3	.04	30.1	7.9k
bcc	5	6.8k	–	639	14.4	.05	44.5	13.9k
bcc	6	28k	–	–	39.6	.09	–	–
fcc	3	108	–	17.4	3.9	.01	4.5	3.5k
fcc	4	256	–	68.8	5.5	.01	12.5	11.5k
fcc	5	500	–	260	9.4	.01	27.7	37.2k
fcc	5	4k	–	1.6k	14.2	.01	110	111k
fcc	4	256k	–	–	1.2k	.58	–	–

<sup>a</sup> Notation: #Sp = number of elemental species.

<sup>b</sup> Notation: #At = total number of atoms in the system.

<sup>c</sup> Speedup ratios: value vs SCRAPs [value vs ATAT in brackets].

<sup>d</sup> ATAT data from Ref. [23]. All times in minutes.

in which MC simulations were performed on a comparable Fe-Mn-Cr-Co system to investigate compositionally-driven SRO [33]. Additionally, our simulation outcomes were consistent with the ordering patterns reported in experimental studies [34, 35] in a  $\text{Fe}_{50}\text{Mn}_{30}\text{Cr}_{10}\text{Co}_{10}$  system.

Employing PyHEA to generate input structures for LAMMPS allowed us to circumvent the extensive MC-MD hybrid computations typically required, which can take several days to complete. PyHEA reduced this computation time to just tens of seconds, showcasing a remarkable improvement in computational efficiency. Further-



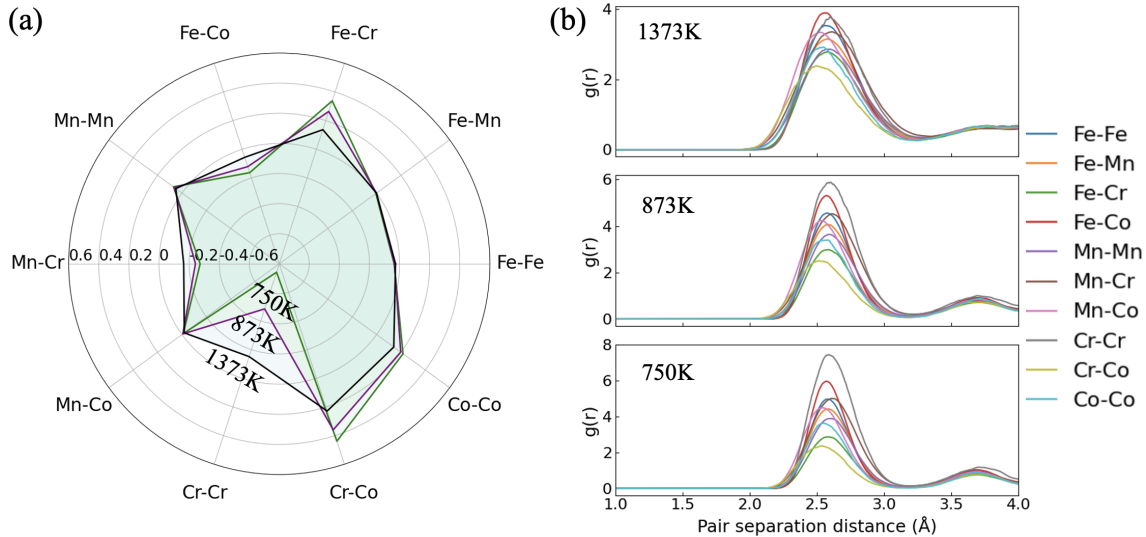


Figure 3: Combined visualization of SRO and radial distribution functions (RDF) for atomic pair interactions at different temperatures. (a) The radar plot illustrates the SRO values for key atomic pairs (e.g., Fe-Fe, Fe-Mn, Fe-Cr) at three temperatures: 750 K, 875 K, and 1373 K. (b) The RDF plots display the spatial distribution of atomic pairs as a function of separation distance (Å) for the same temperatures, with smooth curves representing each pair.

more, the scale of the simulation, involving 256,000 atoms, surpasses the capabilities of most existing methods, emphasizing PyHEA’s robustness and effectiveness in handling large-scale atomistic simulations.

The temperature-dependent evolution of SRO in this system is further illustrated by Fig. A.6 in the Appendix, which presents Warren-Cowley SRO parameter matrices at different temperatures (1373 K, 873 K, and 750 K). These heat maps reveal how the atomic ordering patterns shift from a nearly random distribution at high temperatures (1373 K) to more pronounced local ordering at lower temperatures (750 K), providing valuable insight into the system’s structural evolution.

### 3. Discussion

This study demonstrates PyHEA’s transformative impact on high-entropy alloy modeling through three key achievements. First, PyHEA achieves unprecedented computational efficiency while maintaining high accuracy. Our benchmarks show that PyHEA outperforms traditional tools like ATAT and SCRAPS by several orders of magnitude, delivering speedups of up to  $333,000\times$  and  $13,900\times$  respectively (Table 1). This dramatic improvement in performance does not come at the cost

of accuracy—PyHEA consistently produces more stable and accurate results across various system sizes, as evidenced by the tighter fitness distributions shown in Fig. 2.

Second, PyHEA successfully addresses the scalability challenge that has long constrained HEA modeling. While existing methods become computationally prohibitive beyond a few thousand atoms, PyHEA’s GPU-accelerated framework efficiently handles systems exceeding 256,000 atoms. This capability represents a significant breakthrough, enabling simulations at experimentally relevant scales that were previously inaccessible. The practical impact of this scalability is demonstrated in our Fe-Mn-Cr-Co system simulation, where PyHEA reduced computation time from days to mere seconds while accurately reproducing temperature-dependent SRO patterns documented in previous studies.

Third, PyHEA’s innovative approach to SRO calculations through incremental updates and GPU optimization establishes a new standard for computational efficiency in materials modeling. The incremental SRO algorithm reduces computational overhead by up to 99.6% (Fig. 5), while GPU acceleration delivers over  $1,000\times$  speedup compared to CPU-based calculations. These technical advances make it feasible to conduct large-scale atomistic simulations with unprecedented efficiency, opening new possibilities for materials design and optimization.

The broader implications of PyHEA’s capabilities extend beyond pure computational advancement. The dramatic reduction in simulation time from days to minutes facilitates more iterative and exploratory research approaches. Researchers can now rapidly test hypotheses, adjust parameters, and explore diverse atomic configurations that were previously impractical due to computational constraints. This acceleration of the research cycle has the potential to significantly accelerate the discovery and optimization of new high-entropy alloys.

Furthermore, PyHEA’s success in modeling complex SRO phenomena in large-scale systems provides valuable insights for understanding structure-property relationships in HEAs. The ability to accurately simulate and analyze SRO patterns across different temperatures and compositions, as demonstrated in our Fe-Mn-Cr-Co case study, offers a powerful tool for predicting and optimizing material properties. This capability is particularly crucial given the growing recognition of SRO’s role in determining mechanical and thermal properties of HEAs. Future developments could further enhance PyHEA’s capabilities in several directions. Integration with advanced machine learning models, particularly reinforcement learning approaches, could optimize the search for desired atomic configurations. Expanding the framework to incorporate additional physical properties and interaction models would broaden its applicability across materials science. Additionally, collaborative efforts with experimental teams could strengthen the validation of PyHEA’s predictions

under various thermomechanical conditions.

In conclusion, PyHEA represents a significant advancement in computational materials science, bridging the gap between theoretical understanding and practical simulation of large-scale HEA systems. Its combination of unprecedented computational efficiency, accurate SRO modeling, and scalability to experimentally relevant sizes establishes a new paradigm for materials design and optimization. As the field continues to evolve, PyHEA’s framework provides a robust foundation for future innovations in high-entropy alloy research and development.

## 4. Methods

### 4.1. Global Search

---

**Algorithm 1** Global Search Algorithm

---

**Require:** Fix input and optimization function

**Ensure:** Optimized solution

- 1: Initialize solutions
  - 2: **while** iteration < Global maximum number **do**
  - 3:     Create new solutions randomly
  - 4:     Calculate fitness  $F$  of the solutions
  - 5:     Choose fraction of solutions with best fitness (top solutions)
  - 6:     **for** each solution  $\in$  top solutions **do**
  - 7:         Search using Monte Carlo (Local Search)
  - 8:     **end for**
  - 9:     Discard fraction  $p_a$  of worst solutions
  - 10:     Rank the solutions and find the current best
  - 11: **end while**
  - 12: Return the best solutions
- 

The optimization of atomic configurations in High-Entropy Alloys (HEAs) presents a complex challenge due to the vast solution space. As illustrated by Fig. 4, our global search framework addresses this challenge through an iterative approach that combines systematic exploration with targeted refinement.

As shown in Fig. 4(a), the global search phase is essential for navigating the extensive configuration space of atomic arrangements in HEAs. This phase strikes a balance between exploration and refinement, allowing for the identification of promising regions within the solution space.

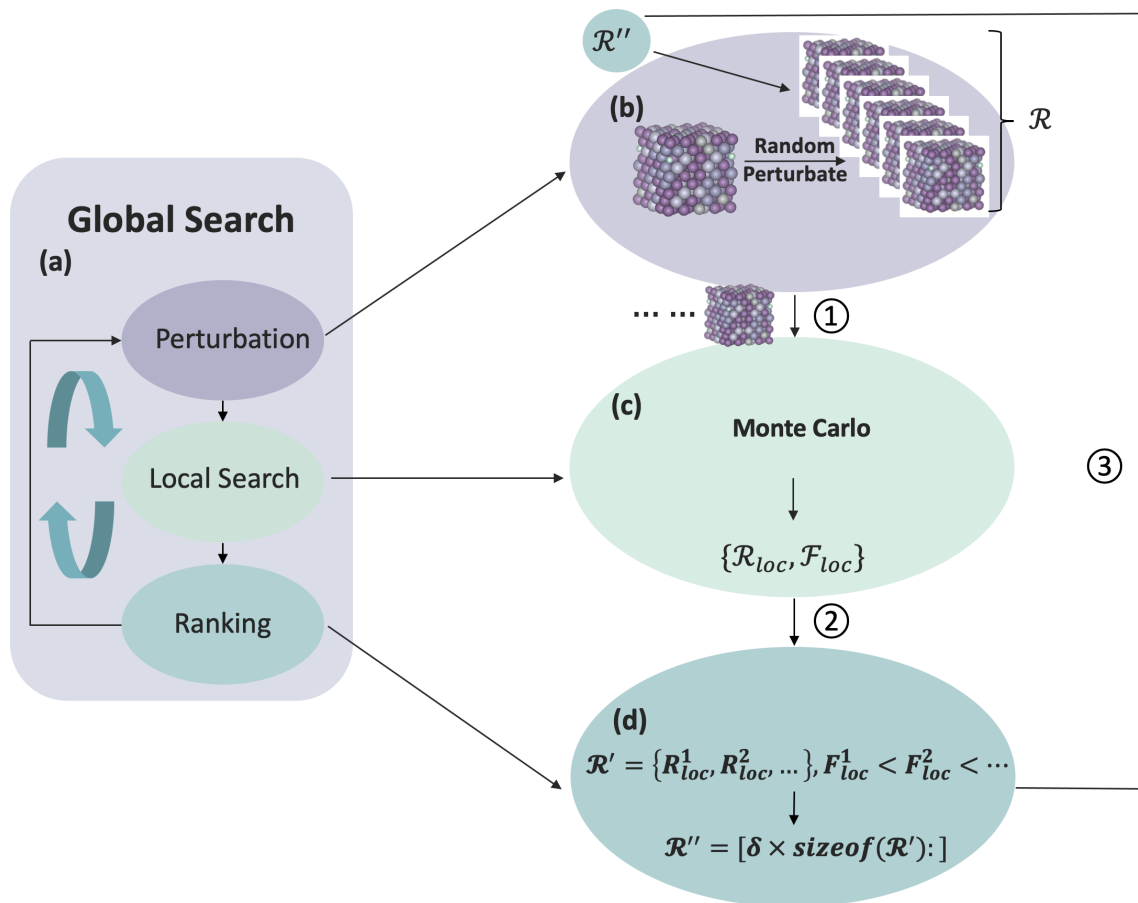


Figure 4: Workflow of the PyHEA algorithm for optimizing atomic configurations. (a) The global search framework iteratively cycles through the stages of perturbation, local search, and ranking to converge toward an optimal solution. (b) Initial atomic configurations consist of randomly generated and previously identified optimal structures for exploration. (c) Monte Carlo (MC) methods are applied to refine each candidate configuration and evaluate their fitness. (d) Configurations are ranked based on fitness, and the lowest-ranked fraction of solutions is discarded to enhance the selection process for subsequent iterations.

The search process begins by generating candidate solutions that represent different atomic configurations (Fig. 4(b)). During each iteration, a subset of solutions undergoes random perturbations to enable broader exploration, while the top-performing configurations are preserved for further refinement (Fig. 4(d)). This approach effectively integrates random exploration with solution improvement.

Drawing inspiration from the Cuckoo Search algorithm, the method employs Lévy flights for optimization [36, 23]. These random jumps facilitate global ex-

ploration and help prevent the algorithm from becoming trapped in local minima. Each candidate solution is evaluated using a fitness function,  $F(X)$ , which quantifies the quality of SRO in the atomic structure by comparing local atomic arrangements to the desired SRO characteristics.

To maintain solution diversity, a portion of low-performing solutions is eliminated at the end of each iteration, while the best solutions are carried forward to the next cycle. This iterative procedure continues until convergence, gradually driving the system toward an optimized atomic configuration with enhanced SRO properties.

#### 4.2. Local Search

---

#### **Algorithm 2** Serial Monte Carlo Search Algorithm

---

**Require:** Fix input and optimization function

**Ensure:** Optimized solution

- 1: Initialize current configuration
  - 2: **while** iteration < Local iterations **do**
  - 3:     Perturb configuration randomly
  - 4:     Calculate fitness difference  $\delta F = F(x) - F(x_{\text{new}})$
  - 5:     **if**  $\delta F < 0$  **or**  $|\delta F| \geq \text{threshold}$  **then**
  - 6:         Restore fitness and configuration to previous state
  - 7:     **end if**
  - 8: **end while**
  - 9: Return the best solutions
- 

The local search phase plays a critical role in refining candidate solutions obtained from the global search phase, particularly in large-scale HEA simulations. To achieve high performance and precision, a parallelized Monte Carlo (MC) search (Alg. 3) is employed, leveraging GPU implementation to efficiently refine atomic configurations in parallel. This parallelization enables the distribution of tasks across multiple threads, where configurations are perturbed, fitness differences are evaluated, and only the highest-performing solutions are retained. This method enhances both computational speed and accuracy, significantly reducing the overall computation time.

Compared to the serial version (Alg. 2), which processes configurations one at a time and struggles with the scalability required for large systems, the parallel approach addresses this limitation by processing multiple configurations simultaneously. This parallelization significantly enhances both scalability and performance. By integrating the parallelized local search with the global search phase, candidate

---

**Algorithm 3** Parallel Monte Carlo Search Algorithm

---

**Require:** Fix input and optimization function

**Ensure:** Optimized solution

- 1: Initialize current configuration
  - 2: **for** each task  $i$  in parallel **do**
  - 3:   Load current fitness and configuration
  - 4:   Perturb configuration randomly
  - 5:   Calculate fitness difference  $\delta F_i = F(x) - F(x_i)$
  - 6:   Synchronize tasks and sort  $\delta F_i$  in descending order
  - 7:   **if**  $\delta F_{min} > 0$  **or**  $|\delta F_{min}| \leq \text{threshold}$  **then**
  - 8:      $depth = 0$
  - 9:     Update current fitness and configuration to  $x_i$
  - 10:   **else**
  - 11:      $depth += 1$
  - 12:   **end if**
  - 13:   **if**  $depth \geq \text{threshold}$  **then**
  - 14:     Break
  - 15:   **end if**
  - 16: **end for**
  - 17: Return the best solutions
- 

solutions are refined to achieve optimal local configurations, facilitating convergence to high-quality results with improved SRO properties.

### 4.3. Short-Range Order

Short-Range Order (SRO) characterizes the local atomic structure in HEAs, describing the tendency of certain atomic species to preferentially cluster compared to a random distribution [37]. The SRO is typically quantified by the Warren-Cowley parameter [9], denoted as  $\alpha_{ij}^k$ , which measures the degree of ordering between atomic species  $i$  and  $j$ . For a given atom  $i$ , the SRO parameter for its  $k$ -th coordination shell is defined as:

$$\alpha_{ij}^k = 1 - \frac{P_{ij}^k}{c_j}, \quad (2)$$

where  $P_{ij}^{(k)}$  is the conditional probability of finding a  $j$  atom in the  $k$ -th coordination shell of an  $i$  atom,  $c_j$  is the overall concentration of  $j$  atoms in the alloy.

The SRO parameter  $\alpha_{ij}^k$  ranges from  $[-1, 1]$ :

- $\alpha_{ij}^k < 0$ : Indicates an attraction between elements  $i$  and  $j$ , suggesting a preference to be adjacent.
- $\alpha_{ij}^k > 0$ : Indicates a repulsion between elements  $i$  and  $j$ , suggesting a preference to be separated.

For each atomic pair type  $(i, j)$ , the SRO parameter for the entire system of  $N$  atoms can be expressed as:

$$\langle \alpha_{ij}^k \rangle = \frac{1}{N_i} \sum_{n=1}^{N_i} \left( 1 - \frac{P_{ij}^k}{c_j} \right), \quad (3)$$

where  $N_i$  is the number of atoms of type  $i$ .

To calculate this parameter, the number of  $j$  atoms within each coordination shell around every  $i$  atom is determined, and the result is normalized by the total concentration of  $j$  atoms ( $c_j$ ). computed SRO values for each pair  $(i, j)$  are then averaged over the entire system to obtain a global measure of the SRO.

#### 4.4. Molecular Dynamics

Molecular dynamics (MD) simulations were performed using LAMMPS [38, 39, 40], employing the 2-NN MEAM potential for the Fe-Mn-Cr-Co alloy system. The simulations encompassed system sizes ranging from 256 to 256,000 atoms, with a timestep of 2 fs in an NPT ensemble. The built-in MC method in LAMMPS was utilized to compute the Radial Distribution Function (RDF), providing detailed insight into the atomic arrangement and SRO.

These simulation parameters were chosen to ensure reproducibility and to facilitate replication in future studies. The results of these MD simulations are discussed in detail in [section 2](#), demonstrating the effectiveness of our method.

#### 4.5. Incremental Calculation of SRO (Fitness)

In the Monte Carlo (MC) search process, the SRO parameter is crucial for evaluating the fitness of each atomic configuration. As previously discussed, SRO quantifies the local atomic arrangement, guiding the search toward optimal configurations during each MC iteration.

In the traditional non-incremental approach, SRO is recalculated from scratch at every MC iteration ([Equation 3](#)). This recalculation becomes increasingly computationally expensive as system size grows. [Fig. 5](#) illustrates that for larger systems, the SRO calculation can consume more than 99% of the total computational cost, highlighting the necessity for a more efficient method.

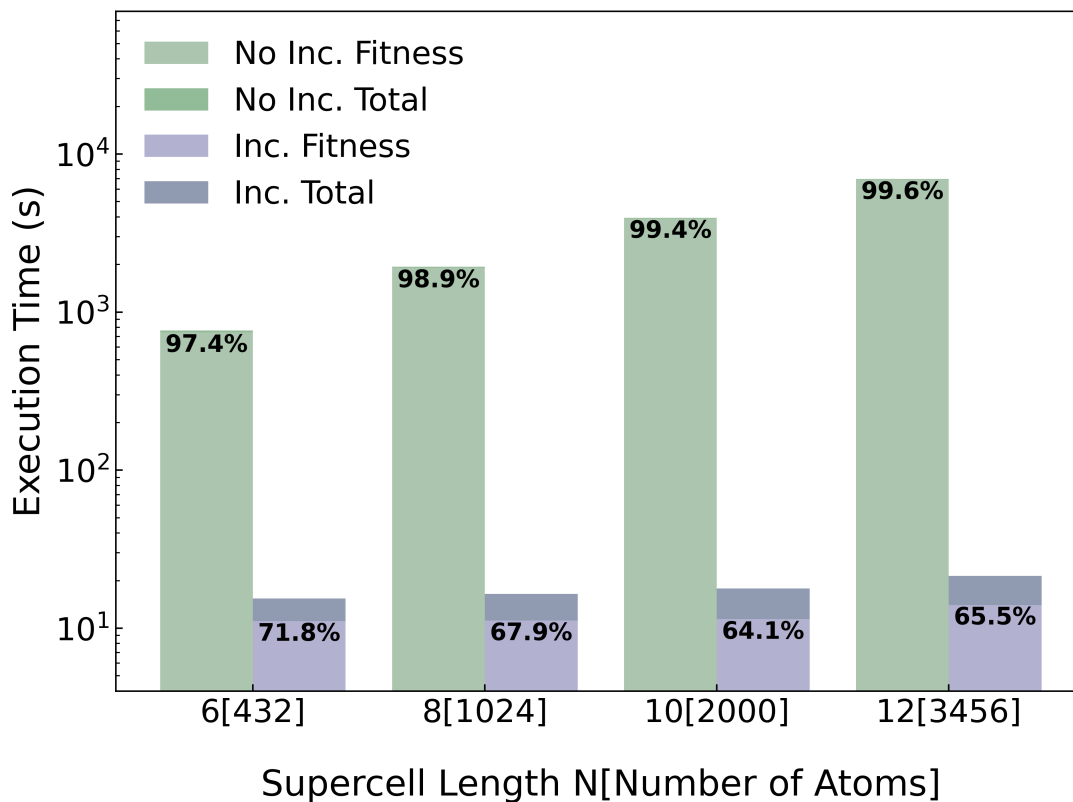


Figure 5: Comparison of execution times for incremental and non-incremental fitness and total calculations in Monte Carlo search. The bar chart shows the execution times (in seconds) for different supercell lengths  $N$  and corresponding atom counts. Incremental methods demonstrate substantial improvements, reducing execution time for both fitness evaluation and total computation. The incremental approach achieves up to a 99.6% reduction in total computation time for larger supercells.



To address this challenge, we implemented an incremental SRO calculation. Instead of recalculating the SRO for the entire system at each iteration, we update only the SRO values influenced by the random swap of two atoms,  $i$  and  $j$ . This approach localizes the update to the environments of the swapped atoms and their neighbors, enabling a more efficient adjustment of the SRO during each MC iteration.

For the incremental update, we first compute the change in SRO for the atoms directly involved in the swap. The change in the SRO value for atom  $i$  and its neighbors is given by:

$$\Delta\alpha_{ij}^k = \left(1 - \frac{P_{ij}^k(\text{new})}{c_j}\right) - \left(1 - \frac{P_{ij}^k(\text{old})}{c_j}\right), \quad (4)$$

where  $P_{ij}^k(\text{new})$  refers to the probability of finding a  $j$  atom in the updated configuration after the swap, and  $P_{ij}^k(\text{old})$  is the corresponding probability before the swap. This incremental approach reduces the computational complexity of each MC iteration from  $O(N)$  to  $O(1)$ , as only the swapped atoms and their neighboring atoms are updated. This improvement is essential for scaling simulations to systems containing hundreds of thousands of atoms without overwhelming computational resources.

Benchmark data shown in Fig. 5 highlights the significant computational burden of non-incremental SRO calculations, which account for 97.4% to 99.6% of the total execution time as system sizes increase from 432 to 3,456 atoms. However, the incremental SRO approach substantially alleviates this burden, reducing total execution times to 71.8% for 432 atoms and stabilizing around 65.5% for larger systems. These findings underscore the incremental method’s ability to enhance computational efficiency and scalability for large-scale HEA simulations.

By adopting incremental SRO updates, we maintain the accuracy of fitness evaluations while significantly reducing the computation time for each MC iteration. This ensures that the MC search process remains efficient and scalable for large-scale HEA simulations.

#### 4.6. GPU Optimization

To further accelerate the MC search and enhance scalability, we implemented a parallel GPU-based optimization. Each thread processes an independent task, and each thread block manages the complete MC search for a single solution. This approach allows the GPU to handle multiple solutions simultaneously, leveraging resources such as registers, shared memory, and low-precision data formats to maximize computational efficiency.

#### 4.6.1. Parallel Processing on the GPU

In this setup, each thread performs the following tasks:

- **SRO Calculation:** Threads compute the SRO for their assigned atomic configurations using low-precision formats (FP16, Uint16) to reduce data footprint and memory access latency, while maintaining sufficient accuracy.
- **Lattice Structure Storage:** The lattice structure [41] is stored in shared memory to minimize memory access time during each MC iteration. This allows all threads within a block to efficiently access and update atomic positions, enhancing computational speed. The lattice structure, derived from the SRO values calculated in registers, is updated following each perturbation:

#### 4.6.2. Iterative Fitness Calculation

Each thread in the block computes the fitness of the perturbed solution during every MC iteration. The fitness, derived from the SRO values calculated in registers, is updated following each perturbation:

$$F_{\text{new}} = F_{\text{prev}} + \Delta F_{\text{perturb}}, \quad (5)$$

where  $\Delta F_{\text{perturb}}$  represents the fitness change from the most recent atomic position perturbation. This value is calculated using the incremental SRO update method.

#### 4.6.3. Fitness Sorting and Selection

After computing the updated fitness in registers, threads within the block collaborate to sort their fitness values using shared memory. The sorting process ensures the rapid identification of the best-performing configuration, which updates the current optimal solution stored in shared memory:

$$F_{\text{best}} = \min(F_{\text{new}}) \quad (6)$$

This guarantees that each block retains the best solution found during the current iteration.

#### 4.6.4. Convergence Check and Termination

The MC search continues iterating until convergence is achieved. Convergence is defined as the point where the fitness of the current best solution shows no significant improvement over a fixed number of steps. Specifically, if  $\Delta F_{\text{best}} = 0$  for a predefined threshold of iterations, the threads within the block terminate the search. The final result, including the atomic configuration and the associated fitness, is then written back to global GPU memory for subsequent analysis.

This GPU-based approach significantly accelerates the MC search by distributing tasks across multiple threads and blocks, enabling the efficient handling of large-scale systems.

## 5. Acknowledgment

This work was conducted under the supervision of Professor Lifeng Liu, School of Integrated Circuits,, Peking University. The author acknowledges the financial support provided by the National Natural Science Foundation of China (Grant No. 61874006).

## 6. Code Availability

The code used for this study is available at <https://github.com/caimeiniu/pyhea>. Access is granted under LGPL-3.0 license.

## Appendix A. Supplementary Data

Table A.2: Performance comparison between PyHEA and existing methods under parallel computing conditions. Both PyHEA and SCRAPs utilized 24 CPU cores (Intel Xeon Gold 6132 @ 2.60GHz) for parallel execution, with additional GPU (single NVIDIA 4090) results shown for PyHEA. The table presents computation times (in minutes) and speedup ratios for both body-centered cubic (bcc) and face-centered cubic (fcc) structures of varying sizes (#At) and species numbers (#Sp). All simulations maintained consistent parameters: 128 candidate solutions, 10 global iterations, 256 MC tasks (depth 10), and supercell sizes following  $S = A \cdot L^3$  where  $A = 2$  (bcc) or  $A = 4$  (fcc). Short-range order was optimized over 3 coordination shells. Dashes (-) indicate computationally infeasible cases, while speedup values are shown relative to SCRAPs[ATAT in brackets].

Type	#Sp <sup>a</sup>	#At <sup>b</sup>	ATAT	SCRAPs Parallel	PyHEA Parallel	PyHEA GPU	Speedup <sup>c</sup>	
							CPU	GPU
bcc	3	54	>1.4k <sup>d</sup>	0.14	0.14	.03	1.0[10k]	4.67[47k]
bcc	4	128	>10k <sup>d</sup>	0.34	0.19	.03	1.79[53k]	11.33[333k]
bcc	4	432	-	1.26	0.28	.03	4.5	42
bcc	4	1024	-	3.18	0.32	.03	9.94	106
bcc	4	2048	-	7.02	0.36	.04	19.5	175.5
bcc	5	2048	-	7.27	0.48	.04	15.2	181.8
bcc	5	6.8k	-	47.4	0.71	.05	66.8	948
bcc	6	28k	-	-	2.05	.09	-	-
fcc	3	108	-	0.63	0.17	.01	3.71	63
fcc	4	256	-	2.24	0.27	.01	8.3	224
fcc	5	500	-	5.81	0.43	.01	13.5	581
fcc	5	4k	-	64.3	0.65	.01	99.0	6.4k
fcc	4	256k	-	-	61.1	.58	-	-

<sup>a</sup> Notation: #Sp = number of elemental species.

<sup>b</sup> Notation: #At = total number of atoms in the system.

<sup>c</sup> Speedup ratios: value vs SCRAPs [value vs ATAT in brackets].

<sup>d</sup> ATAT data from Ref. [23]. All times in minutes.

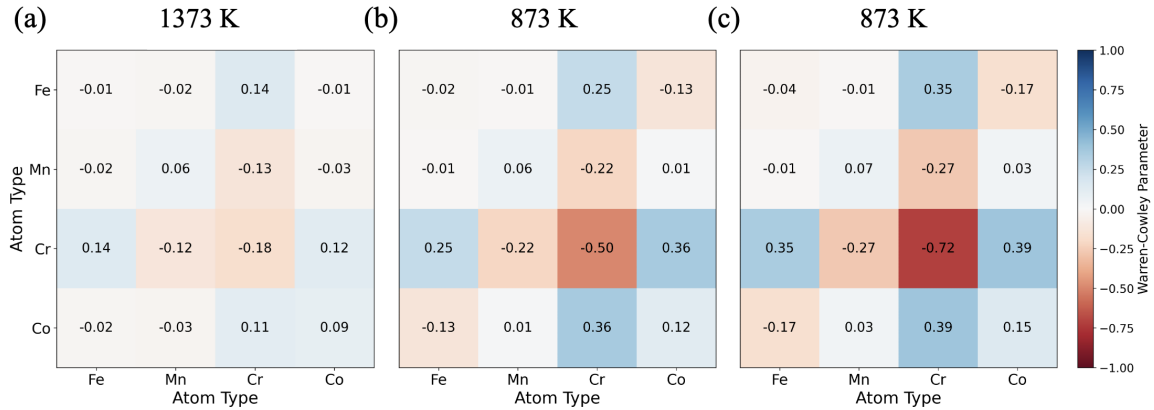


Figure A.6: Warren-Cowley SRO parameter matrices for a multi-principal-element alloy (Fe, Mn, Cr, Co) at three different temperatures: (a) 1373 K, (b) 873 K, and (c) 873 K. The color scale ranges from blue (positive values) to red (negative values), indicating a preference for certain atom types to cluster together (positive SRO) or to avoid each other (negative SRO). At high temperatures (1373 K), the SRO values are near zero, reflecting a more random distribution, whereas at lower temperatures (873 K), the emergence of pronounced SRO patterns reveals stronger local atomic ordering.

## References

- [1] J.-W. Yeh, S.-K. Chen, S.-J. Lin, J.-Y. Gan, T.-S. Chin, T.-T. Shun, C.-H. Tsau, S.-Y. Chang, Nanostructured high-entropy alloys with multiple principal elements: novel alloy design concepts and outcomes, *Advanced engineering materials* 6 (5) (2004) 299–303.
- [2] D. B. Miracle, O. N. Senkov, A critical review of high entropy alloys and related concepts, *Acta materialia* 122 (2017) 448–511.
- [3] E. P. George, D. Raabe, R. O. Ritchie, High-entropy alloys, *Nature reviews materials* 4 (8) (2019) 515–534.
- [4] W. Li, D. Xie, D. Li, Y. Zhang, Y. Gao, P. K. Liaw, Mechanical behavior of high-entropy alloys, *Progress in Materials Science* 118 (2021) 100777.
- [5] J. W. Yeh, Y. L. Chen, S. J. Lin, S. K. Chen, High-entropy alloys—a new era of exploitation, in: *Materials science forum*, Vol. 560, Trans Tech Publ, 2007, pp. 1–9.
- [6] Y. Zhang, T. T. Zuo, Z. Tang, M. C. Gao, K. A. Dahmen, P. K. Liaw, Z. P. Lu, Microstructures and properties of high-entropy alloys, *Progress in materials science* 61 (2014) 1–93.

- [7] Z. Li, K. G. Pradeep, Y. Deng, D. Raabe, C. C. Tasan, Metastable high-entropy dual-phase alloys overcome the strength–ductility trade-off, *Nature* 534 (7606) (2016) 227–230.
- [8] Y. Zhang, X. Yang, P. Liaw, Alloy design and properties optimization of high-entropy alloys, *Jom* 64 (2012) 830–838.
- [9] J. M. Cowley, An approximate theory of order in alloys, *Physical Review* 77 (5) (1950) 669.
- [10] D. De Fontaine, Cluster approach to order-disorder transformations in alloys, in: *Solid state physics*, Vol. 47, Elsevier, 1994, pp. 33–176.
- [11] Q. Ding, Y. Zhang, X. Chen, X. Fu, D. Chen, S. Chen, L. Gu, F. Wei, H. Bei, Y. Gao, et al., Tuning element distribution, structure and properties by composition in high-entropy alloys, *Nature* 574 (7777) (2019) 223–227.
- [12] R. Zhang, S. Zhao, J. Ding, Y. Chong, T. Jia, C. Ophus, M. Asta, R. O. Ritchie, A. M. Minor, Short-range order and its impact on the crconi medium-entropy alloy, *Nature* 581 (7808) (2020) 283–287.
- [13] Y. Han, H. Chen, Y. Sun, J. Liu, S. Wei, B. Xie, Z. Zhang, Y. Zhu, M. Li, J. Yang, et al., Ubiquitous short-range order in multi-principal element alloys, *Nature Communications* 15 (1) (2024) 6486.
- [14] E. Pickering, N. Jones, High-entropy alloys: a critical assessment of their founding principles and future prospects, *International Materials Reviews* 61 (3) (2016) 183–202.
- [15] S. Chen, Z. H. Aitken, S. Pattamatta, Z. Wu, Z. G. Yu, D. J. Srolovitz, P. K. Liaw, Y.-W. Zhang, Simultaneously enhancing the ultimate strength and ductility of high-entropy alloys via short-range ordering, *Nature communications* 12 (1) (2021) 4953.
- [16] X. Liu, W. Curtin, Atomistic simulations reveal strength reductions due to short-range order in alloys, *Acta Materialia* 263 (2024) 119471.
- [17] A. Ferrari, F. Körmann, M. Asta, J. Neugebauer, Simulating short-range order in compositionally complex materials, *Nature Computational Science* 3 (3) (2023) 221–229.

- [18] C. Zhang, Y. Yang, The calphad approach for heas: Challenges and opportunities, *MRS Bulletin* 47 (2) (2022) 158–167.
- [19] J.-W. Yeh, Alloy design strategies and future trends in high-entropy alloys, *Jom* 65 (2013) 1759–1771.
- [20] M. He, W. J. Davids, A. J. Breen, S. P. Ringer, Quantifying short-range order using atom probe tomography, *Nature Materials* 23 (9) (2024) 1200–1207.
- [21] G. Ghosh, A. Van de Walle, M. Asta, First-principles calculations of the structural and thermodynamic properties of bcc, fcc and hcp solid solutions in the al–tm (tm= ti, zr and hf) systems: a comparison of cluster expansion and supercell methods, *Acta Materialia* 56 (13) (2008) 3202–3221.
- [22] A. van de Walle, The alloy-theoretic automated toolkit (atat): A user guide, Brown University, Providence, RI, Tech. Rep (2019).
- [23] R. Singh, A. Sharma, P. Singh, G. Balasubramanian, D. D. Johnson, Accelerating computational modeling and design of high-entropy alloys, *Nature Computational Science* 1 (1) (2021) 54–61.
- [24] S. Yin, J. Ding, M. Asta, R. O. Ritchie, Ab initio modeling of the energy landscape for screw dislocations in body-centered cubic high-entropy alloys, *npj Computational Materials* 6 (1) (2020) 110.
- [25] J. Cohen, M. Fine, Some aspects of short-range order, *J. Phys. Radium* 23 (10) (1962) 749–762.
- [26] S. Zhao, Local ordering tendency in body-centered cubic (bcc) multi-principal element alloys, *Journal of Phase Equilibria and Diffusion* 42 (5) (2021) 578–591.
- [27] R. Salloom, M. I. Baskes, S. G. Srinivasan, Atomic level simulations of the phase stability and stacking fault energy of fecocrmnsi high entropy alloy, *Modelling and Simulation in Materials Science and Engineering* 30 (7) (2022) 075002.
- [28] X. Liu, J. Zhang, Z. Pei, Machine learning for high-entropy alloys: Progress, challenges and opportunities, *Progress in Materials Science* 131 (2023) 101018.
- [29] I. Toda-Caraballo, J. S. Wróbel, D. Nguyen-Manh, P. Pérez, P. Rivera-Díaz-del Castillo, Simulation and modeling in high entropy alloys, *JOM* 69 (2017) 2137–2149.

- [30] J. Rickman, G. Balasubramanian, C. Marvel, H. Chan, M.-T. Burton, Machine learning strategies for high-entropy alloys, *Journal of applied physics* 128 (22) (2020).
- [31] V. Sorkin, S. Chen, T. L. Tan, Z. Yu, M. Man, Y. Zhang, First-principles-based high-throughput computation for high entropy alloys with short range order, *Journal of Alloys and Compounds* 882 (2021) 160776.
- [32] P. A. Santos-Florez, S.-C. Dai, Y. Yao, H. Yanxon, L. Li, Y.-J. Wang, Q. Zhu, X.-X. Yu, Short-range order and its impacts on the bcc monobinary multi-principal element alloy by the machine-learning potential, *Acta Materialia* 255 (2023) 119041.
- [33] J. B. Seol, W.-S. Ko, S. S. Sohn, M. Y. Na, H. J. Chang, Y.-U. Heo, J. G. Kim, H. Sung, Z. Li, E. Pereloma, et al., Mechanically derived short-range order and its impact on the multi-principal-element alloys, *Nature communications* 13 (1) (2022) 6766.
- [34] Y. Wu, F. Zhang, X. Yuan, H. Huang, X. Wen, Y. Wang, M. Zhang, H. Wu, X. Liu, H. Wang, et al., Short-range ordering and its effects on mechanical properties of high-entropy alloys, *Journal of Materials Science & Technology* 62 (2021) 214–220.
- [35] D. Liu, Q. Wang, J. Wang, X. Chen, P. Jiang, F. Yuan, Z. Cheng, E. Ma, X. Wu, Chemical short-range order in Fe<sub>50</sub>Mn<sub>30</sub>Co<sub>10</sub>Cr<sub>10</sub> high-entropy alloy, *Materials Today Nano* 16 (2021) 100139.
- [36] X.-S. Yang, S. Deb, Cuckoo search via Lévy flights, in: 2009 World congress on nature & biologically inspired computing (NaBIC), IEEE, 2009, pp. 210–214.
- [37] F. Zhang, S. Zhao, K. Jin, H. Xue, G. Velisa, H. Bei, R. Huang, J. Ko, D. Pagan, J. Neumeier, et al., Local structure and short-range order in a NiCoCr solid solution alloy, *Physical review letters* 118 (20) (2017) 205501.
- [38] J. Li, Q. Fang, B. Liu, Y. Liu, Y. Liu, Mechanical behaviors of AlCrFeCuNi high-entropy alloys under uniaxial tension via molecular dynamics simulation, *RSC advances* 6 (80) (2016) 76409–76419.
- [39] Y. Afkham, M. Bahramyan, R. T. Mousavian, D. Brabazon, Tensile properties of AlCrFeCuNi glassy alloys: A molecular dynamics simulation study, *Materials Science and Engineering: A* 698 (2017) 143–151.



- [40] Y. Tang, D. Li, Nano-tribological behavior of high-entropy alloys crmnfeconi and crfeconi under different conditions: A molecular dynamics study, *Wear* 476 (2021) 203583.
- [41] U. Dahlborg, J. Cornide, M. Calvo-Dahlborg, T. Hansen, A. Fitch, Z. Leong, S. Chambreland, R. Goodall, Structure of some cocrfeni and cocrfenipd multicomponent hea alloys by diffraction techniques, *Journal of Alloys and Compounds* 681 (2016) 330–341.
- [42] U. Dahlborg, J. Cornide, M. Calvo-Dahlborg, T. Hansen, A. Fitch, Z. Leong, S. Chambreland, R. Goodall, Efficient stochastic generation of special quasirandom structures, *Journal of Alloys and Compounds* 681 (2016) 330–341.